A Very Long Baseline Array Trigonometric Parallax for RR Aql and the Mira Period–Luminosity Relation

Yan Sun[1,2] , Bo Zhang[1] , Mark J. Reid[3] , Shuangjing Xu[1,4], Shiming Wen[1], Jingdong Zhang[1,2], and Xingwu Zheng[5]
[1] Shanghai Astronomical Observatory, Chinese Academy of Sciences 80 Nandan Road, Shanghai 200030, People's Republic of China; zb@shao.ac.cn
[2] University of Chinese Academy of Sciences, No.19 (A) Yuquan Rd. Shijingshan, Beijing 100049, People's Republic of China
[3] Center for Astrophysics | Harvard & Smithsonian, 60 Garden Street, Cambridge, MA 02138, USA
[4] Korea Astronomy and Space Science Institute, 776 Daedeok-daero, Yuseong-gu, Daejeon 34055, Republic of Korea
[5] School of Astronomy and Space Science, Nanjing University 22 Hankou Road, Nanjing 210093, People's Republic of China
Received 2021 December 24; revised 2022 April 17; accepted 2022 April 22; published 2022 May 26

Abstract

We report Very Long Baseline Array observations of 22 GHz H_2O and 43 GHz SiO masers toward the Mira variable RR Aql. By fitting the SiO maser emission to a circular ring, we estimate the absolute stellar position of RR Aql and find agreement with Gaia astrometry to within the joint uncertainty of ≈ 1 mas. Using the maser astrometry we measure a stellar parallax of 2.44 ± 0.07 mas, corresponding to a distance of 410^{+12}_{-11} pc. The maser parallax deviates significantly from the Gaia EDR3 parallax of 1.95 ± 0.11 mas, indicating a 3.8σ tension between radio and optical measurements. This tension is most likely caused by optical photocenter variations limiting the Gaia astrometric accuracy for this Mira variable. Combining infrared magnitudes with parallaxes for RR Aql and other Miras, we fit a period–luminosity relation using a Bayesian approach with Markov Chain Monte Carlo sampling and a strong prior for the slope of -3.60 ± 0.30 from the Large Magellanic Cloud. We find a K-band zero-point (defined at $\log P(\text{days}) = 2.30$) of -6.79 ± 0.15 mag using very long baseline interferometry (VLBI) parallaxes and -7.08 ± 0.29 mag using Gaia parallaxes. The Gaia zero-point is statistically consistent with the more accurate VLBI value.

1. Introduction

Mira variables in the Large Magellanic Cloud (LMC) show a well-defined period–luminosity relation (PLR) in the infrared (Glass & Lloyd Evans 1981; Whitelock et al. 2008; Yuan et al. 2017; Iwanek et al. 2021a). Assuming the PLR slope from the LMC, zero-points of the PLRs for Miras have also been determined in other galaxies, e.g., M33 (Yuan et al. 2018), NGC 4258 (Huang et al. 2018), and NGC 1559 (Huang et al. 2020). Compared with Cepheids, Miras are brighter at infrared wavelengths (Feast & Whitelock 2014) and have a larger range of ages and greater numbers (Eyer & Cuypers 2000). Miras can also provide distances rivaling those of Cepheids (Iwanek et al. 2021a). Thus, Miras will be important in the era of large space infrared telescopes, e.g., the James Webb Space Telescope (JWST). However, there are some issues regarding the use of the PLR of Miras that need to be addressed. First, more observational evidence that the PLR of Miras in different galaxies is insensitive to metallicity variations is desirable. Second, if the PLR of Miras is universal, the zero-point for the PLR should be better determined. Third, using the PLR of LMC Miras to estimate distances to other galaxies includes a component of systematic error due to the assumed distance to the LMC; currently the most accurate distance modulus of 18.477 ± 0.026 mag was published by Pietrzyński et al. (2019).

The Gaia Early Data Release 3 (EDR3) provides parallaxes for more than 1000 Miras with formal uncertainties of $\leqslant 0.5$ mas. This provides an opportunity to derive a Galactic PLR for Miras independently of the LMC. Thus, it is important to check the Gaia parallaxes with independent methods of comparable or better accuracy, e.g., using very long baseline interferometry (VLBI). As shown in Xu et al. (2019), there are significant discrepancies between the parallaxes from Gaia and VLBI for Miras. One likely reason for these discrepancies involves optical photocenter variations, owing to a small number of very large convective cells (Chiavassa et al. 2011) or hot spots (Lacour et al. 2009). Since Miras typically have diameters of ≈ 2 au (Willson 1981), which imply angular sizes of twice their parallaxes, photocenter variations of, say, 10% could lead to astrometric noise of 20% of a parallax. To further complicate this problem, Miras typically have periods near 1 yr (Willson 1981), and thus photocenter variations can easily correlate with a yearly parallax signature.

In order to determine the PLR for Galactic Miras, accurate parallaxes for five Miras have been obtained with Very Long Baseline Array (VLBA) observations and 17 have been obtained with the VLBI exploration of radio astrometry (VERA), as part of a key project started in 2004 (Nakagawa 2009; VERA Collaboration et al. 2020). Since the total number of VLBI parallaxes for Miras is modest, adding more is important. RR Aql is an oxygen-rich Mira with a period of 396 days with strong circumstellar OH (the hydroxyl radical), H_2O, and SiO masers (Benson et al. 1990). Although its trigonometric parallax has been estimated optically by Hipparcos (van Leeuwen 2007) and in the radio by observations of its OH masers (Vlemmings & van Langevelde 2007), the uncertainties in these measurements are too large to be useful as a check on Gaia. In this paper, we present VLBI parallax measurements of 22 GHz H_2O and 43 GHz SiO maser emission toward RR Aql using the VLBA. In Section 2, we describe the observations

Table 1
Positions and Brightnesses

Source Name (1)	R.A. (J2000) (K / Q) (h m s) (2)	Decl. (J2000) (K / Q) (° ′ ″) (3)	S_p (K / Q) (Jy/beam) (4)	θ_{sep} (°) (5)	P.A. (°) (6)	V_{LSR} (K / Q) (km s^{-1}) (7)	Beam (K / Q) (mas mas °) (8)
RR Aql	19 57 36.0334 / 36.0377	−01 53 12.157 / 12.203	6 / 13	⋯	⋯	28.9 / 30.9	3.49 × 1.3 @ +22 / 1.85×0.6 @ +23
J1947−0103	19 47 43.7837	−01 03 24.528	0.167 / 0.042	2.60	+159	⋯	3.48×1.2 @ +22 / 1.74 × 0.6 @ +23

Note. K and Q denote the observing bands, ∼22 GHz for the H$_2$O maser and ∼43 GHz for the SiO maser, respectively. The second and third columns list the absolute positions of the H$_2$O maser spot at V_{LSR} = 28.9 km s^{-1} and of the SiO maser spot at V_{LSR} = 30.9 km s^{-1} on 2018 January 9. The fourth and seventh columns give the peak brightnesses (S_p) and V_{LSR} of the maser spots. The fifth and sixth columns give the separations (θ_{sep}) and position angles (P.A.) east of north of the quasar relative to the maser. The last column gives the FWHM size and P.A. of the Gaussian restoring beam at the first epoch. The quasar position is from http://astrogeo.org.

and analysis procedures. In Section 3, we present the positions of both H$_2$O and SiO maser spots in RR Aql relative to extragalactic quasars at different epochs and the derived parallaxes and proper motions. In Section 4, we compare the absolute positions of Gaia and our VLBI results. Then in Section 5, we fit a PLR using the VLBI and Gaia parallaxes separately, using a Bayesian approach with Markov Chain Monte Carlo (MCMC) sampling, which avoids hand-editing of data by decreasing the penalty in the likelihood function for outliers compared to using a Gaussian data uncertainty. Finally, we summarize our studies and discuss the future outlook for the PLR of Miras in Section 6.

2. Observation and Data Reduction

We conducted phase-referenced observations of RR Aql (α_{J2000} = 19^{h}57^{m}36^{s}0334/36^{s}0377, δ_{J2000} = −01°53′12″157/12″203 for H$_2$O/SiO masers, see Table 1 for details) relative to a background quasar J1947−0103 (α_{J2000} = 19^{h}47^{m}43^{s}7837, α_{J2000} = −01^{s}03′24″528) at 22 and 43 GHz under the National Radio Astronomy Observatory's[6] VLBA program BZ069. These observations included six epochs spanning about 1 yr from 2017 October 29 to 2018 November 2 at intervals of roughly 2 months. An observation on 2018 August 21 failed with no detections of any quasars or masers on all of the interferometer baselines; the reason for the failure is unknown. Each epoch used a 6 hr track that included multiple observing blocks of 25 minutes of fast-switching between RR Aql and a background quasar J1947−0103.[7] Scan durations for the maser source were 60 and 40 s, yielding typical on-source times of 40 and 20 s at 22 and 43 GHz, respectively. For better interferometer UV-coverage at each band, we alternated the fast-switching blocks at 22 and 43 GHz. The data were taken in left- and right-circular polarizations with four adjacent bands of 16 MHz bandwidth, with the maser emission placed in the third band.

We observed three International Celestial Reference Frame sources: 3C345, 1638+572, and 1740+521 at the beginning, middle, and end of the observations, in order to calibrate electronic delay and phase offsets among different bands. In order to calibrate tropospheric delays, we adopted the methods described in Reid et al. (2009). We included three 0.5 hr "geodetic blocks" at the beginning, middle, and end of tracks. Geodetic blocks were recorded in left-circular polarization with eight 16 MHz bands spanning 480 MHz between 23.5 and 24.0 GHz. The eight

bands were spaced in a "minimum redundancy configuration" to uniformly sample frequency differences.

The data were correlated in two passes using the DiFX software correlator (Deller et al. 2007) in Socorro, NM. One pass generated 32 spectral channels for all the data, and another pass generated 1000 spectral channels (in "zoom" mode) only for the single (dual-polarized) frequency band containing the masers, yielding spectral channels spaced by 8 kHz, corresponding to velocity resolutions of 0.11 and 0.06 km s^{-1} for H$_2$O and SiO maser emissions, respectively.

Data calibration and imaging were performed using the Astronomical Image Processing System (AIPS; van Moorsel et al. 1996). For phase calibration, we corrected for the effects of diurnal feed rotation, errors in the Earth orientation parameters, and the positions of the masers and the background source adopted in the correlation. We removed instrumental delays using the data from 3C345 and calibrated ionospheric and tropospheric delays using the global ionospheric model, provided by the International GNSS Service, and data from the geodetic blocks (Reid & Honma 2014). For amplitude calibration, we adopted the VLBA's recommended system equivalent flux densities for each antenna and feed, using gain curves and system temperatures.

As shown in Figure 1, we found strong H$_2$O and SiO maser emissions with peaks at the velocity of local standard rest (V_{LSR}) values of around 29 and 31 km s^{-1} for all epochs. In this paper, we measure parallax using the maser channels centered at 28.8 and 28.9 km s^{-1} for H$_2$O masers and 30.9 km s^{-1} for the SiO masers. Since the water maser emissions were heavily resolved on the longer baselines, we phase-referenced those data using the quasar J1947−0103 and only used the data from the VLBA inner-five antennas: Fort Davis (FD), Kitt Peak (KP), Los Alamos (LA), Owens Valley (OV), and Pie Town (PT). These antennas are located close to the center of the array, with relatively short baselines. However, on 2017 October 29, there were clock jumps at the PT antenna, which were evident in plots of interferometric delay versus time using the strongest calibrator, and we discarded the data involving PT. In addition, the PT antenna was unavailable for the observation on 2017 December 31 owing to a maintenance issue. For the SiO masers, we used the 30.9 km s^{-1} maser spot as the interferometer phase reference (i.e., "inverse" phase-referencing).

After calibration, we combined the four dual-polarized bands and imaged the continuum emission of the background source using the AIPS task IMAGR, which Fourier transforms the visibility data to make a brightness image. The restoring beam for each epoch was calculated using uniform weighting. In individual spectral channels, we estimated peak brightnesses, positions, and angular sizes using the task JMFIT, which fits

---

[6] The National Radio Astronomy Observatory is a facility of the National Science Foundation operated under cooperative agreement by Associated Universities, Inc.

[7] Another quasar, J2001−0042, was also observed, but proved too weak to use.
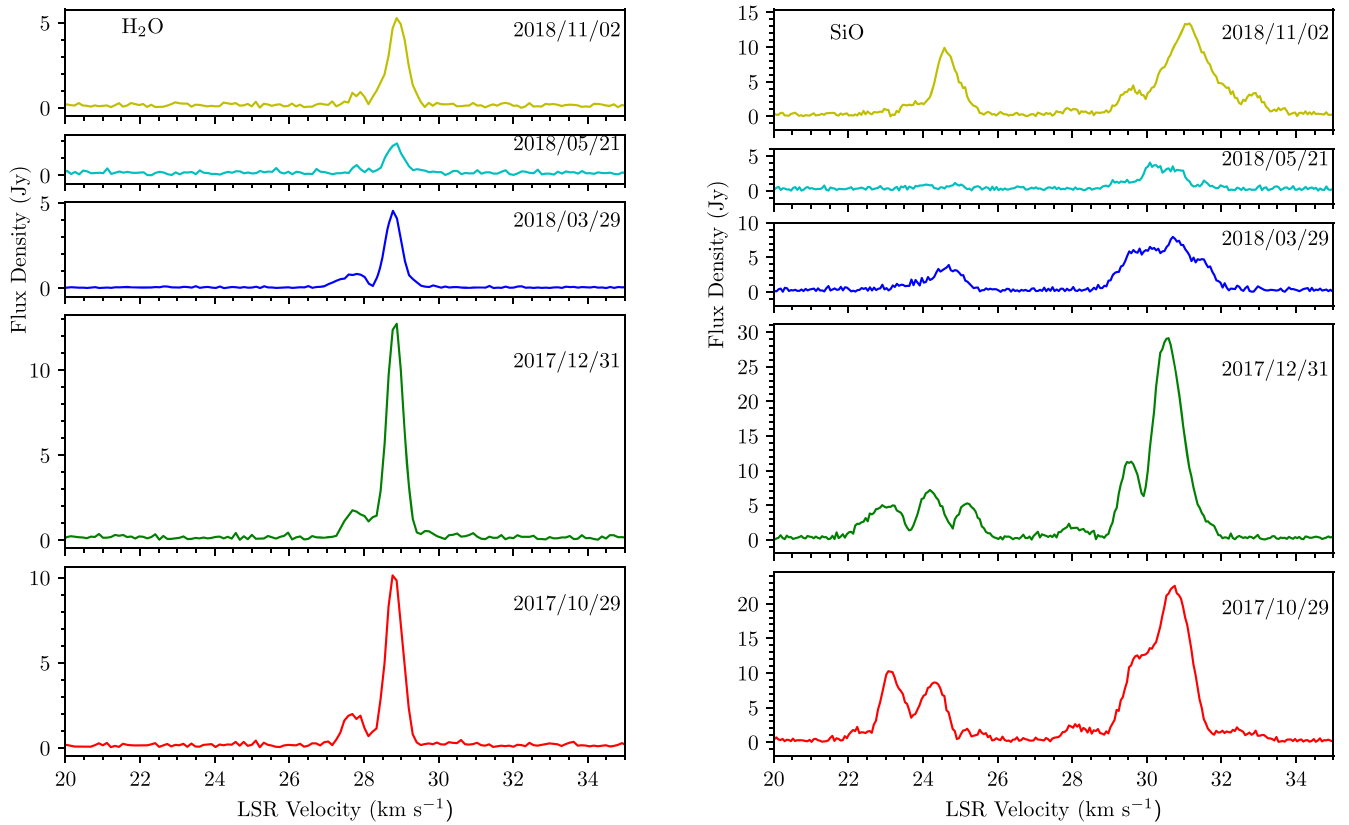
Figure 1. Vector-averaged interferometer spectra of H_2O (*left panel*) and SiO (*right panel*) maser emission toward RR Aql from the Kitt Peak to Los Alamos baseline at five epochs.

Gaussian brightness distributions to a portion of an image. Table 1 lists basic information for the observed sources, and Table 2 gives the measured residual position offsets for the maser spots relative to the quasar J1947–0103 used for parallax fitting. Figure 2 shows an example image of the H_2O maser spots at $V_{LSR} = 28.8$ km s^{-1} and 28.9 km s^{-1} toward RR Aql and the background source J1947–0103.

3. Results

3.1. Maser Spots Identification for Astrometry

3.1.1. Water Masers

As shown in Figure 3, the phase variations of the reference source J1947–0103 on 2018 March 29, as an example, are relatively slow; thus the phases on the baselines of the inner-five VLBA antennas can be confidently connected without 2π ambiguities between adjacent scans separated by 2 minutes.

Water maser emission was detected at V_{LSR} of 27.9 km s^{-1} from 2017 October 29 to 2018 March 29. However, by 2018 May 21 its brightness fell below 0.4 Jy beam^{-1} and was not detected. This is not unusual for maser emission from Miras, which also vary over the stellar period. For parallax measurement, we focus on analyzing the stronger water maser spots at V_{LSR} of 28.8 and 28.9 km s^{-1}, which were clearly detected at all epochs. Figure 4 shows the evolution of the 28.9 km s^{-1} maser spot relative to the calibrator J1947–0103. On 2018 March 29 we detected strong emission at (E,N) of $\approx(-5, -20)$ mas (left panel) and weaker emission at $\approx(80, -55)$ mas (right panel). Clearly the weaker spot is unrelated to those tracking smoothly toward the south–southwest over the five epochs. Therefore, we excluded the weaker spot from our

parallax fitting. On 2018 November 2 the maser emission displays a head-tail-like structure. This is probably due to blending two maser spots separated by several mas. Parallax fitting with one or the other spot position clearly shows that the stronger "head" spot is the continuation of the previous four epochs.

3.1.2. SiO Masers

As shown in the right panel of Figure 1, the SiO masers have more features than the H_2O masers: There are at least a handful of SiO features at V_{LSR} ranging from 23 to 31 km s^{-1}. After phase-referencing to the maser spot at V_{LSR} of 30.9 km s^{-1}, we made the velocity-integrated images shown in Figure 5. There are clear indications of a clumpy ringlike structure at the first three epochs; in later epochs the western part of the ring weakens and vanishes. Fortunately, maser feature A was detected at all epochs, and we used this feature to determine the parallax of RR Aql.

3.2. Parallax and Proper Motion

As described in Section 3.1, we used two H_2O and one SiO maser spot detected in all five epochs spanning 1 yr. The positions of maser spots relative to the background source were modeled by the parallax sinusoid in both coordinates (determined by one parameter) and a linear proper motion in each coordinate, and best parameter values were obtained by variance-weighted least-squares fitting. The formal position uncertainties listed in Table 2 reflect thermal (random) noise in the interferometric images and do not include systematic uncertainties. To estimate and allow for systematic position

Table 2
Residual Position Differences between Maser Spots and J1947−0103 Used for the Parallax Fits

Epoch (yyyy/ mm/dd) (1)	Maser Species (2)	V_{LSR} (km s^{-1}) (3)	East Offset (mas) (4)	North Offset (mas) (5)
2017/ 10/29	H$_2$O	28.9	0.043 ± 0.080	-0.051 ± 0.133
2017/ 12/31			-2.242 ± 0.060	-8.407 ± 0.102
2018/3/29			-4.543 ± 0.129	-17.096 ± 0.180
2018/5/21			-8.113 ± 0.111	-24.495 ± 0.194
2018/11/2			-22.480 ± 0.186	-46.289 ± 0.238
2017/ 10/29	H$_2$O	28.8	-1.067 ± 0.061	-6.565 ± 0.113
2017/ 12/31			-3.112 ± 0.052	-15.165 ± 0.094
2018/3/29			-5.850 ± 0.138	-24.830 ± 0.215
2018/5/21			-9.058 ± 0.131	-31.472 ± 0.238
2018/11/2			-23.535 ± 0.199	-53.031 ± 0.242
2017/ 10/29	SiO	30.9	23.945 ± 0.038	50.273 ± 0.069
2017/ 12/31			21.800 ± 0.054	41.297 ± 0.097
2018/3/29			19.286 ± 0.052	30.119 ± 0.107
2018/5/21			15.468 ± 0.132	26.109 ± 0.243
2018/11/2			1.125 ± 0.069	0.736 ± 0.153

Note. The first column lists the observing epochs. The second and third columns list the maser species and their V_{LSR}. The fourth and fifth columns give position offsets relative to $\alpha_{J2000} = 19^h57^m36^s.0337$, $\delta_{J2000} = -01°53'12''.148$ for the H$_2$O masers on 2017 October 29, and $\alpha_{J2000} = 19^h57^m36^s.0364$, $\delta_{J2000} = -01°53'12''.242$ for the SiO maser on 2018 November 2. Uncertainties given are statistical only, based on thermal noise in the images, and do not include systematic effects such as uncompensated atmospheric delays.

errors caused by residual atmospheric delays and variable structure of the maser spots and/or the background quasar, we added "systematic errors" (error floors) for each coordinate in quadrature with the formal measurement errors and adjusted these to reach a reduced χ^2 for the post-fit residuals near unity for each coordinate.

Figure 6 shows the positions of the two H$_2$O spots and one SiO spot relative to the background source J1947−0103, with superposed curves showing the best-fit parallax sinusoid. Note that the error bars in the bottom panel are larger than those in the top panel, indicating the "error floors" for the north–south offsets were larger than those for the east–west offsets. This occurs because the interferometer beams are larger in the north–south direction and uncompensated atmospheric delays are more correlated with them. Table 3 lists the individual fits (for each maser spot) and a combined fit (using all three spots), allowing for different offsets and proper motions among them.

For the combined fits using both H$_2$O and SiO masers, to avoid a single error floor down-weighting the better H$_2$O maser data, we combined measurement uncertainties with the error floors used in the individual fits (multiplied by 0.8) in revised data files, in order to get a reduced chi-square near unity. The parallax fitting results are in good agreement within their joint measurement uncertainties. Considering that the dominant error is from uncompensated atmospheric delays, which are

essentially the same for all spots and both maser species, we conservatively inflated the formal parallax uncertainty by $\sqrt{3}$ (for the three spots combined). We adopt the parallax from the combined fits, which is 2.44 ± 0.07 mas, corresponding to a distance of 410^{+12}_{-11} pc. We find that the maser parallax deviates significantly from the Gaia EDR3 parallax of 1.95 ± 0.11 mas, indicating a 3.8σ tension between radio and optical astrometry. We discuss possible reasons for this discrepancy in Section 4.

4. Stellar Position of RR Aql

4.1. Relative Positions of Masers Respect to the Central Star of RR Aql

The absolute stellar positions of Miras determined from VLBI observations can be used to check the optical Gaia positions, which might be corrupted by nonuniform circumstellar dust extinction and photocenter variation. Additionally, knowing the position of masers relative to the central stars can be crucial to understanding gas kinematics in the circumstellar material.

As shown in Figure 5, the sky distribution of SiO masers from our VLBA observations at the first three epochs show a clumpy ringlike structure. This has previously been noted for H$_2$O maser emission (e.g., from W Hya by Reid & Menten 1991) and SiO maser emission (e.g., from TX Cam by Kemball & Diamond 1997). We fit the central position (assumed to be the stellar position) and the radius of a ring to the maser positions using a least-square method described by Yoon et al. (2018), which assumes the distribution of SiO masers lie at a common radius from the central star. The fitted results are shown in Table 4.

Figure 7 shows relative positions of masers respect to the central star on 2017 October 29. Adopting a stellar radius (R_*) of 3.8 ± 0.3 mas for RR Aql from multi-epoch mid-infrared interferometric observations by Karovicova et al. (2011), we conclude that the SiO masers are distributed near 2 R_*, while the H$_2$O maser emission at $V_{LSR} = 28.8$ km s^{-1} and 28.9 km s^{-1} is located $\approx$18 R_* northwest of the central star. This is consistent with previously reported circumstellar maser distributions by Reid & Menten (1997) and Richards et al. (2010).

4.2. Comparison of the Absolute Position of RR Aql from VLBA and Gaia

In order to evaluate differences between optical photocenters and radio measurements, we compare the absolute positions of the center of the SiO ring with stellar positions from Gaia (see Table 4). At the first three epochs the SiO masers have a well-constrained ring structure, which gives very accurate positions for the central star. Table 5 shows the differences between our radio and the Gaia optical stellar positions (using Gaia's five astrometric parameters listed in EDR3); joint uncertainties are estimated by adding the individual values in quadrature. There are no statistically significant differences in either the R.A. or decl. components. We note that uncertainty in the optical to radio celestial frame-link also contributes to the position differences; there is approximately a 1 mas difference in the orientation of radio and optical frame when measured at brighter magnitudes between the Gaia DR2 and VLBI data of 26 radio stars (Lindegren 2020).

The Gaia EDR3 "astrometric excess noise" value, which measures the disagreement between the observations and the best-fitting astrometric model, is 0.84 mas for RR Aql. As pointed out
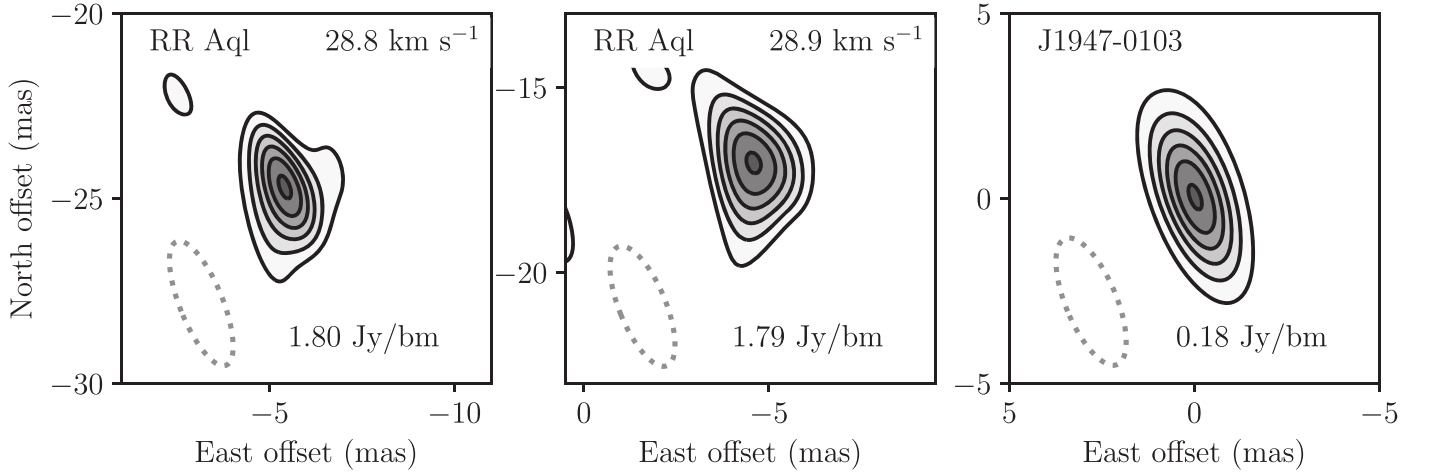
Figure 2. Images of the H_2O maser spots at $V_{LSR} = 28.8$ km s^{-1} (*left panel*) and $V_{LSR} = 28.9$ km s^{-1} (*middle panel*) toward RR Aql and the background radio source J1947−0103 (*right panel*) on 2018 March 29 using the inner-five antennas of the VLBA. The restoring beams are shown in the lower left corner of each panel. Contour levels are spaced linearly by 0.25 Jy beam^{-1} for RR Aql and 0.030 Jy beam^{-1} for J1947–0103.
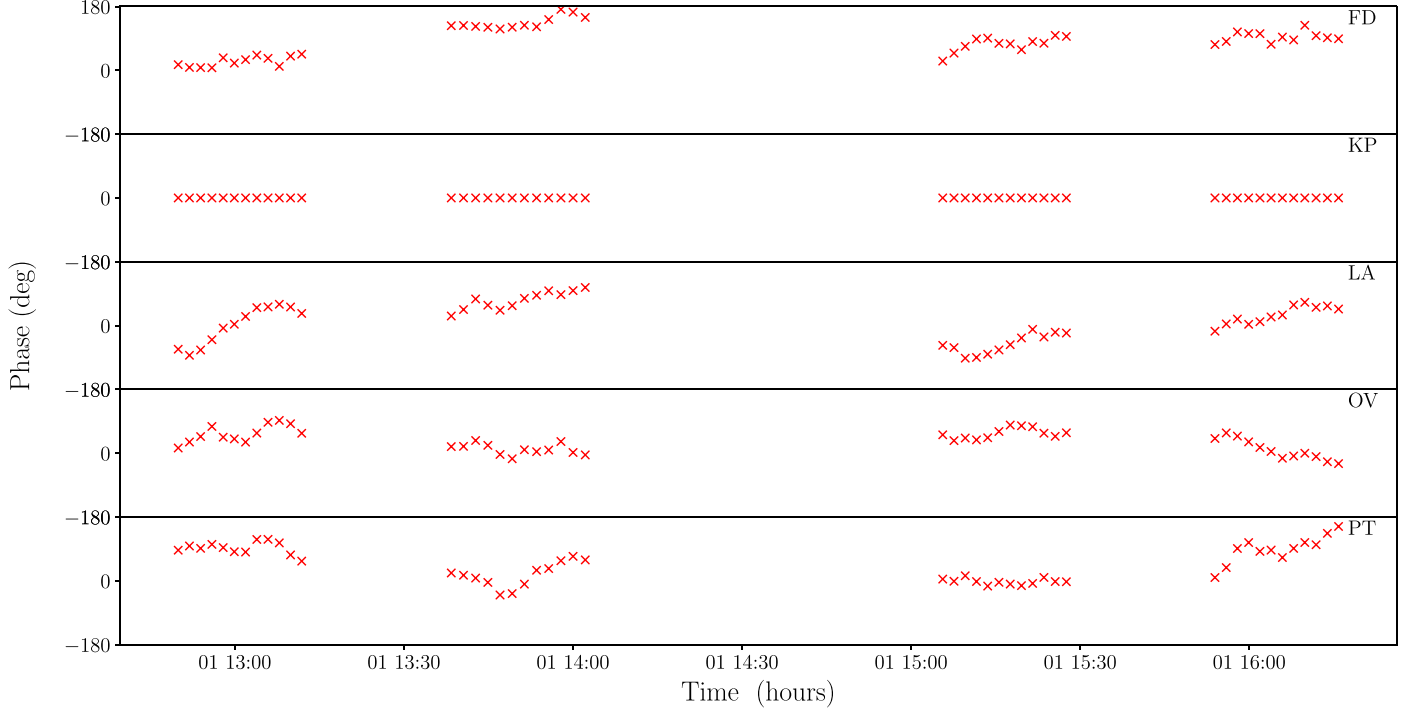
Figure 3. Visibility phase vs. observing time of calibrator J1947–0103 at 22 GHz on 2018 March 29. The two-letter station codes of the VLBA inner-five antennas are labeled on the top-right corner in each panel. FD, KP, LA, OV, and PT indicate Fort Davis, Kitt Peak, Los Alamos, Owens Valley, and Pie Town, respectively. The reference station was KP. The interval between adjacent data points is 2 minutes.

by Lindegren et al. (2021), this noise not only includes the effect of the photocenter variability, but can also come from modeling errors (e.g., from excess attitude noise of the Gaia satellite). However, assuming modeling errors are small, it is likely that photocenter variability would be near the astrometric excess noise value, which is ≈15% of its angular diameter. This is possible, since as shown in the optical interferometric image of the Mira variable χ Cyg by Lacour et al. (2009), a single hot spot can offset to the stellar center by up to 30% of its diameter.

5. Mira Period–Luminosity Relation

As pointed out by Wood (2000), Miras are radial fundamental-mode pulsators, while semiregular variables (SRVs) can pulsate in the fundamental mode and/or in overtones. Pulsation periods of SRVs can be hard to determine accurately, since as their name indicates they often are not regular. Hence, we focus only on Miras in this paper. For RR Aql, in order to determine its location on the PLR diagram, we estimated a primary period of 396 ± 5 days (see the left panel of Figure 8) using the visual data from 1904 November to 2021 August and the data analysis tool VStar provided by the American Association of Variable Star Observers (AAVSO),[8] using the date compensated discrete Fourier transform (DCDFT) algorithm (Ferraz-Mello 1981), which corresponds to a maximum likelihood sinusoidal-plus-constant regression curve fitting.

_____
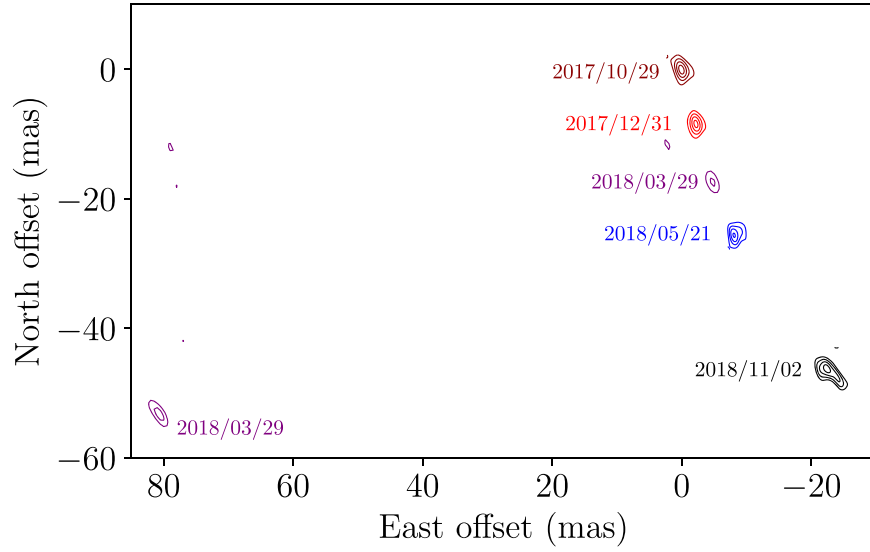
Figure 4. Spatial distribution of the H$_2$O maser emission at $V_{\mathrm{LSR}} = 28.9$ km s^{-1} toward RR Aql from VLBA observations at five epochs. The observing epoch is labeled next to each maser spot. Contour levels are integer multiples of 10% of the peak brightness. Note that on 2018 March 29 two maser features are detected.
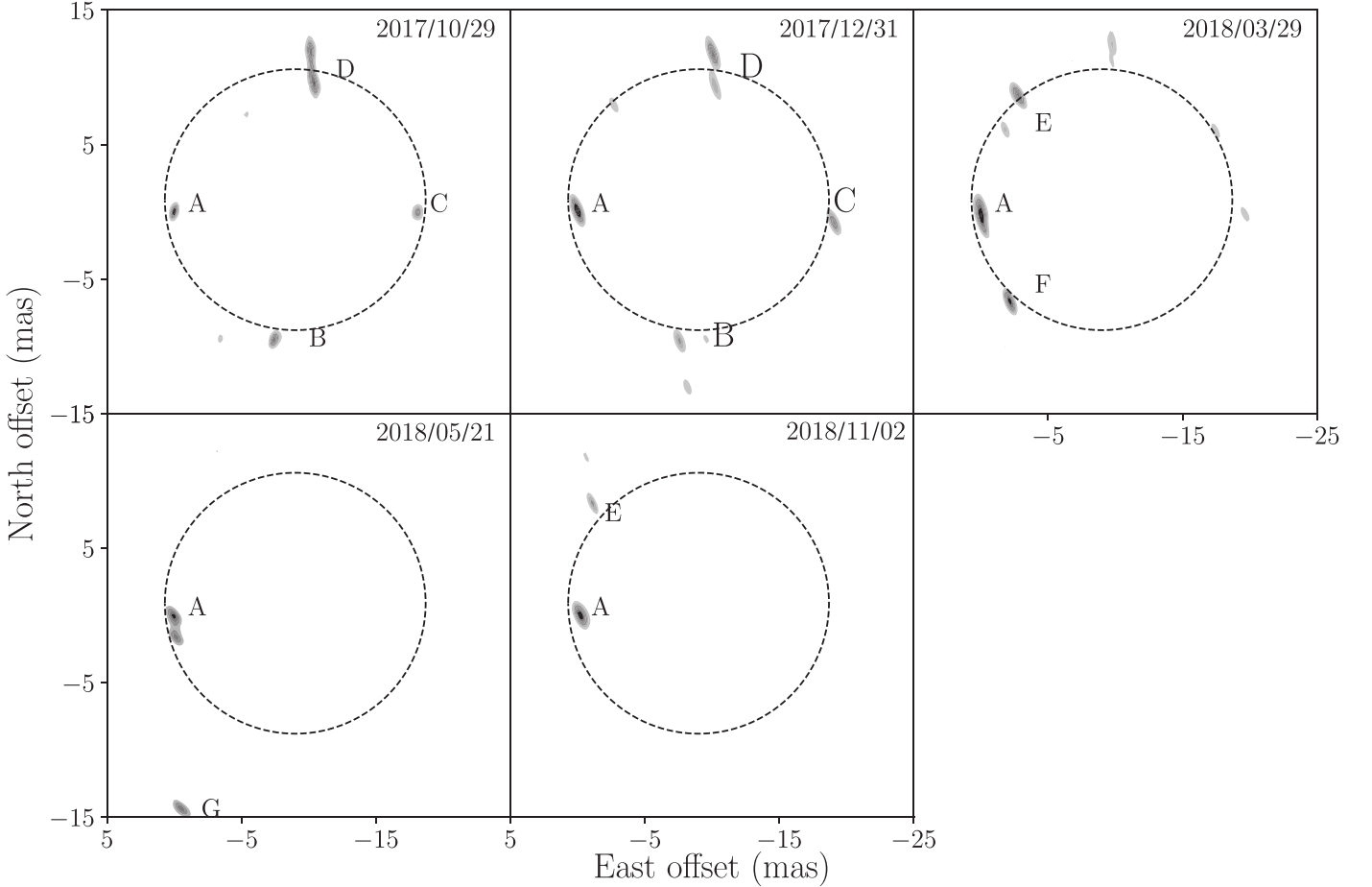
Figure 5. Spatial distributions of SiO maser spots toward RR Aql from VLBA observations at five epochs. Maser features are designated with letters. The long-lived feature A was used for parallax estimation. The dashed circles denote rings fitted to the SiO maser emissions.

Compared to a DFT, the DCDFT provides a better estimation of the power spectrum of a time series with uneven spacing. The right panel of Figure 8 shows a phase-folded visual light curve of RR Aql using the period of 396 days.

The apparent magnitude at an effective wavelength of 2.2 μm for RR Aql ($m_K = 0.84 \pm 0.26$ mag) comes from the Two Micron All Sky Survey (2MASS) point-source catalog. Since Miras vary by upwards of 1 mag at 2 μm and 2MASS

6
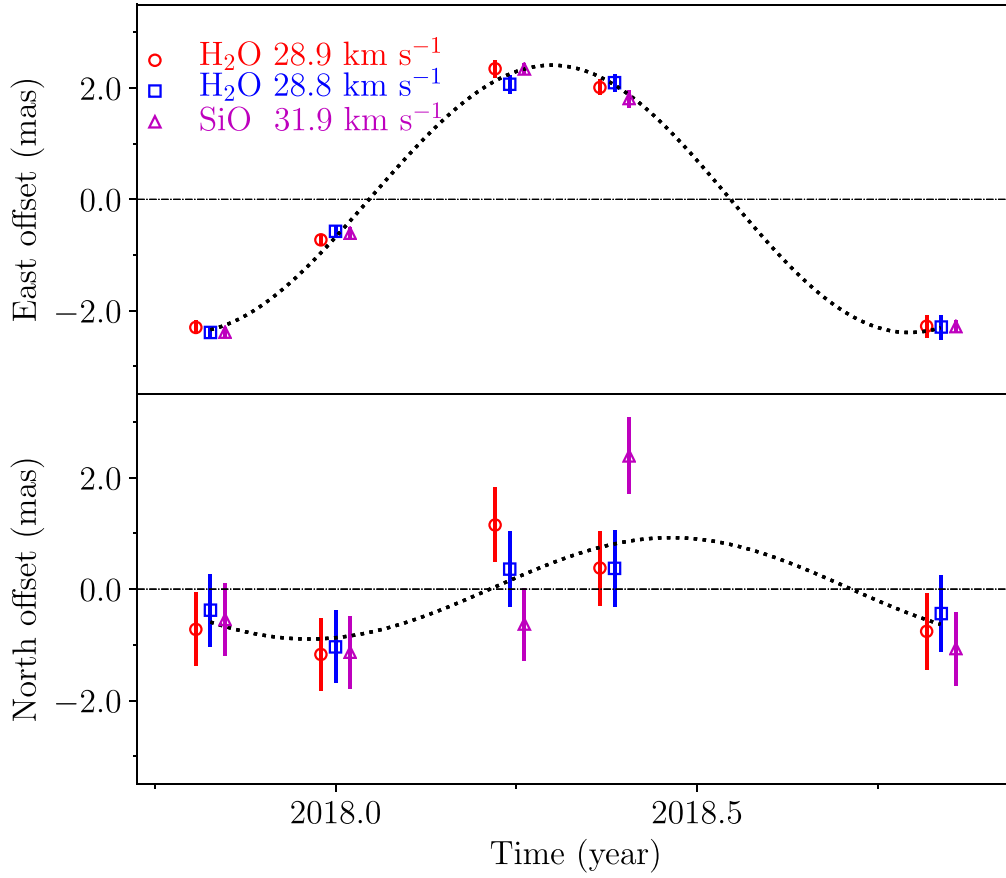
Figure 6. East (*upper panel*) and north (*lower panel*) offsets relative to J1907−0103 vs. time used for parallax fitting for two H_2O maser spots *(blue squares and red circles)* and one SiO maser spot *(purple triangle)*, with individual constant offset and proper motion removed. The V_{LSR} of each maser spot is labeled on the left-top corner in the upper panel. The best-fitting model *(dotted lines)* denotes the common parallax curve. Positions are slightly offset in time for clarity.

Table 3
Parallax and Proper Motion for RR Aql

Method	V_{LSR} (km s^{-1})	Parallax (mas)	μ_x (mas yr^{-1})	μ_y (mas yr^{-1})	Δx (mas)	Δy (mas)	χ_ν^2	σ_x (mas)	σ_y (mas)
H_2O	28.9	2.44 ± 0.07	-22.29 ± 0.17	-45.70 ± 0.85	-8.94 ± 0.05	-22.43 ± 0.30	0.83	0.00	0.70
H_2O	28.8	2.41 ± 0.09	-22.29 ± 0.23	-45.91 ± 0.46	-9.96 ± 0.08	-29.39 ± 0.17	0.96	0.09	0.31
SiO	30.9	2.44 ± 0.08	-22.68 ± 0.18	-48.47 ± 1.46	14.86 ± 0.07	26.33 ± 0.52	0.98	0.13	1.14
Combined		2.44 ± 0.07					0.98	0.00	0.00
Gaia EDR3		1.95 ± 0.11	-20.42 ± 0.12	-47.69 ± 0.08					

Note. Absolute proper motions are defined as $\mu_x = \mu_\alpha \cos \delta$ and $\mu_y = \mu_\delta$. Position offsets Δx and Δy are for 2018 May 1 (the midpoint between the first and last epochs) and are relative to the positions listed in Table 1; χ_ν^2 is the reduced χ^2 of post-fit residuals, σ_x and σ_y are error floors in x and y, respectively. "H_2O" and "SiO" denote the maser species; "combined" means the parameters derived by combing the data of the two H_2O and one SiO maser spots. The last row lists the parameters from Gaia EDR3.

Table 4
Center Position and Radius of SiO Maser Ring

Epoch (yyyy/mm/dd) (1)	α_{J2000} (h m s) (2)	σ_α (mas) (3)	δ_{J2000} (° ′ ″) (4)	σ_δ (mas) (5)	Radius (mas) (6)
2017/10/29	19 57 36.03728	± 0.3	$-01\ 53\ 12.1908$	± 1.2	10.0 ± 0.1
2017/12/31	19 57 36.03715	± 0.3	$-01\ 53\ 12.1997$	± 1.2	9.9 ± 0.1
2018/3/29	19 57 36.03797	± 0.3	$-01\ 53\ 12.2100$	± 1.2	10.2 ± 0.2

Note. Columns 2 through 5 list the absolute positions and uncertainties in R.A. and decl. of the center of the SiO maser ring. Column 6 lists the best-fit radii of SiO maser rings.
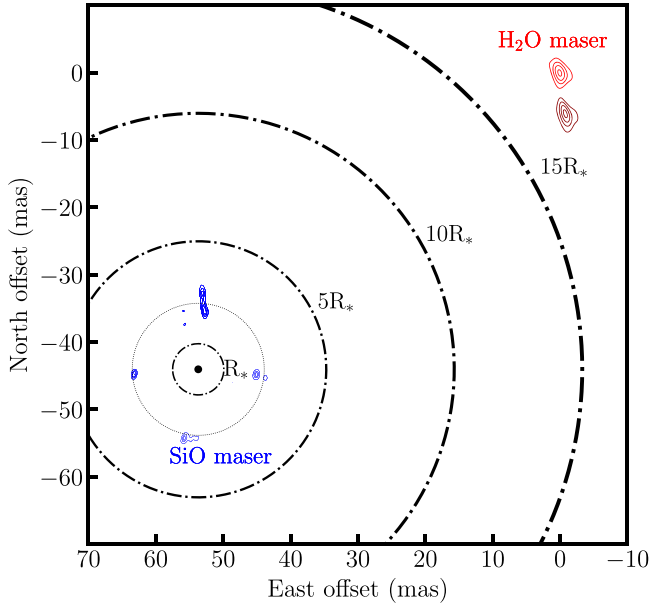
Figure 7. The sky distribution SiO and H$_2$O masers with respect to the central star of RR Aql on 2017 October 29. The dotted line represents the fitted SiO maser ring. The circles in dashed–dotted lines indicate multiples of five stellar radii.

Table 5
Differences in Positions of RR Aql from Gaia EDR3 and VLBA

Epoch (yyyy/mm/dd) (1)	R.A. Difference (mas) (2)	Decl. Difference (mas) (3)	2D Difference (mas) (4)
2017/10/29	-0.22 ± 0.41	0.59 ± 1.19	0.63 ± 1.26
2017/12/31	0.58 ± 0.42	1.00 ± 1.20	1.16 ± 1.27
2018/3/29	-0.49 ± 0.44	0.64 ± 1.20	0.81 ± 1.28

Note. The position differences are calculated by subtracting the values of VLBA measurements from those of Gaia EDR3, based on fitting a ring to the SiO maser spot distributions. Columns 1, 2, and 3 list the R.A., decl. differences, and the two-dimensional position differences.

measurements are only at one epoch, this leads to extra uncertainty in the mean magnitude owing to periodic variations. In order to better estimate a mean apparent magnitude at near-infrared K-band, we adopted a method similar to those demonstrated in Yuan et al. (2018) and Iwanek et al. (2021b). This involved converting a modeled optical light curve to a near-infrared one using an amplitude ratio ($A_K/A_V = 0.21 \pm 0.09$) and a phase-lag ($\Delta\Phi_{KV} = 0.10 \pm 0.07$) between the two (Iwanek et al. 2021b); then we added an infrared phase-adjusted constant (-0.44 mag) to the measured magnitude. The mean magnitude for RR Aql using the lightcurve correction method is 0.40 ± 0.33 mag. Figure 9 shows an example of the lightcurve correction to mean magnitude for RR Aql. We estimate the uncertainty of $m_K^{\rm mean}$ by taking into account the uncertainties from both $m_K^{\rm 2MASS}$ and the amplitude ratio, and phase-lag for lightcurve correction.

Table 6 lists all Miras with both VLBI and Gaia parallaxes so that we could fit PLR parameters separately for comparison. Where available, we adopted mean magnitudes $m_K^{\rm Kagoshima}$ of time-monitored m_K measurements from the Kagoshima University 1 m telescope, which used between 18 and 38 epochs per star.

Otherwise we used $m_K^{\rm mean}$ estimated with one-epoch 2MASS data by the lightcurve correction method as done for RR Aql. Absolute magnitudes of Miras at near-infrared K-band (M_K) were estimated by adopting the parallax results from Gaia and VLBI maser observations, separately. The uncertainties in the absolute magnitudes, M_K, take into account uncertainties of both m_K and the parallax measurements used to convert from apparent to absolute magnitude. All values used for Miras with both VLBI and Gaia parallaxes to fit Galactic PLRs are listed in Table 6.

It is clear from Figure 10 that, while a reasonable PLR is evident using either VLBI or Gaia parallaxes, there are some clear outliers. Rather than remove outliers "by eye", which has the potential for significant bias, in order to fit a PLR we use a Bayesian approach with MCMC sampling, which intrinsically handles outliers without bias. Specifically we adopt the "conservative formulation" of Sivia & Skilling (2006), for which the probability distribution function for the uncertainty of a datum, σ, is given by

$$\mathrm{prob}(\sigma|\sigma_0, I) = \sigma_0/\sigma^2,$$

where σ_0 is a (Gaussian) uncertainty of a "good" datum such that $\sigma \geqslant \sigma_0$. Marginalizing over the unknown σ, leads to a likelihood function proportional to $\ln\left[\dfrac{1 - e^{-R^2/2}}{R^2}\right]$, where $R = (D - M)/\sigma_0$ and D and M are the datum and model values. Unlike a Gaussian likelihood, this function has Lorentzian-like tails, which assigns a significant probability to multi-σ_0 outliers. As prior information for our fits, we adopt a slope of -3.60 ± 0.30 and a zero-point defined at $\log P(\text{days}) = 2.30$ of -6.90 ± 1.00 mag. Our fitted Mira PLR parameters are listed in Table 7. We note that the VLBI parallaxes yield nearly a factor of two smaller uncertainty than the Gaia parallaxes.

As shown by Iwanek et al. (2021a) and Iwanek et al. (2021b), a sample of O-rich Miras with a large period range clearly show a nonlinear PLR, while a sample restricted to $\log P \approx 2.0$–2.8 can be well described by a linear PLR. To compare our Galactic PLR with an even smaller range of $\log P$ from ≈ 2.4–2.8 to the existing PLRs in literature, we list only the latest determined linear PLR of O-rich Miras measured at near-infrared K-band for different galaxies in Table 7. Yuan et al. (2017) determined a linear PLR based on about 160 O-rich Miras with periods <400 days at near-infrared wavelengths, and we adjusted the zero-point using the updated distance modulus of 18.477 ± 0.026 mag for the LMC from Pietrzyński et al. (2019). We took account of uncertainties from both the photometric zero-point (~ 0.02 mag) and distance modulus (~ 0.03 mag), which were not included in Yuan et al. (2017). The linear PLR for M 33 (Yuan et al. 2018) is from near-infrared light curves of 1169 O-rich Miras with periods <400 days assuming a slope of -3.77, which is the same as the LMC value from Yuan et al. (2017). In addition, assuming a distance modulus of 18.477 ± 0.026 mag from Pietrzyński et al. (2019), Iwanek et al. (2021b) determined the PLR of Miras in the LMC at near-infrared K-band using a sample of 29 O-rich Miras.

Since we rely on a strong prior for the slope of the PLR, we now only compare zero-points for the LMC and M 33 and with Milky Way values based on VLBI and Gaia calibrations. It is clear that the PLR zero-points of the LMC and M 33 derived by Yuan et al. (2017, 2018) differ by only 0.05 mag and are consistent with each other. The zero-points for the Milky Way based on VLBI and Gaia parallaxes are statistically consistent
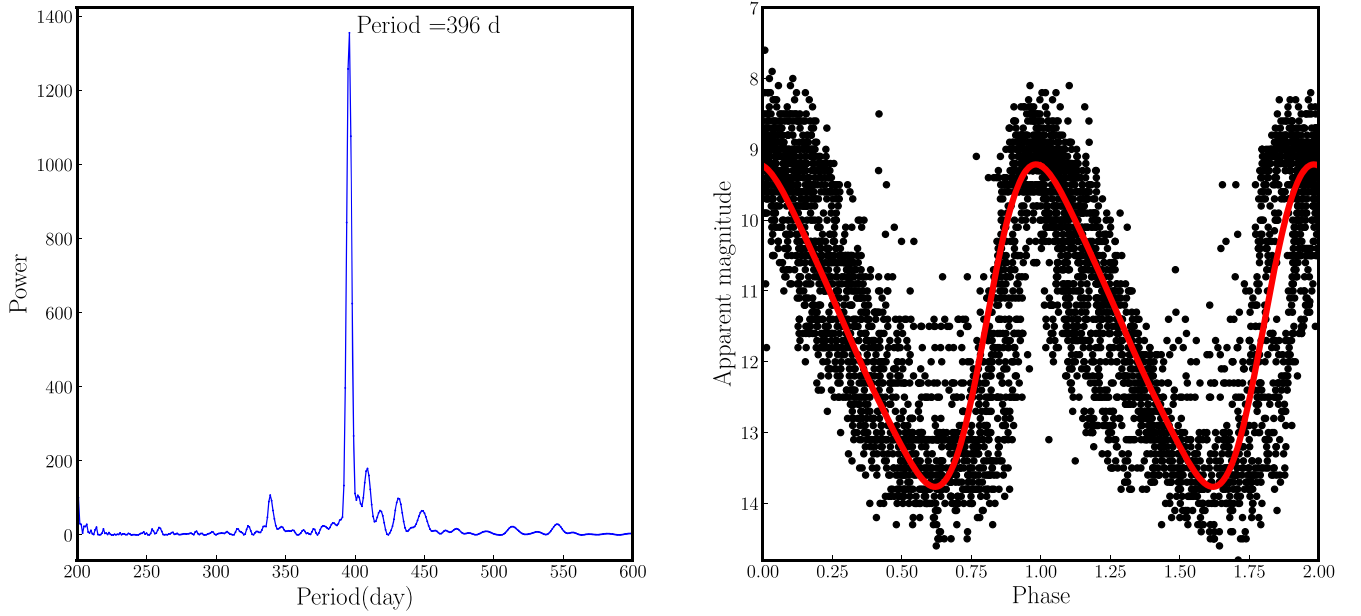
Figure 8. Period analysis result (*left panel*) and phase-folded light curve (*right panel*) of the visual data from 1904 November to 2021 August for RR Aql. A pulsating period of 396 days is found.
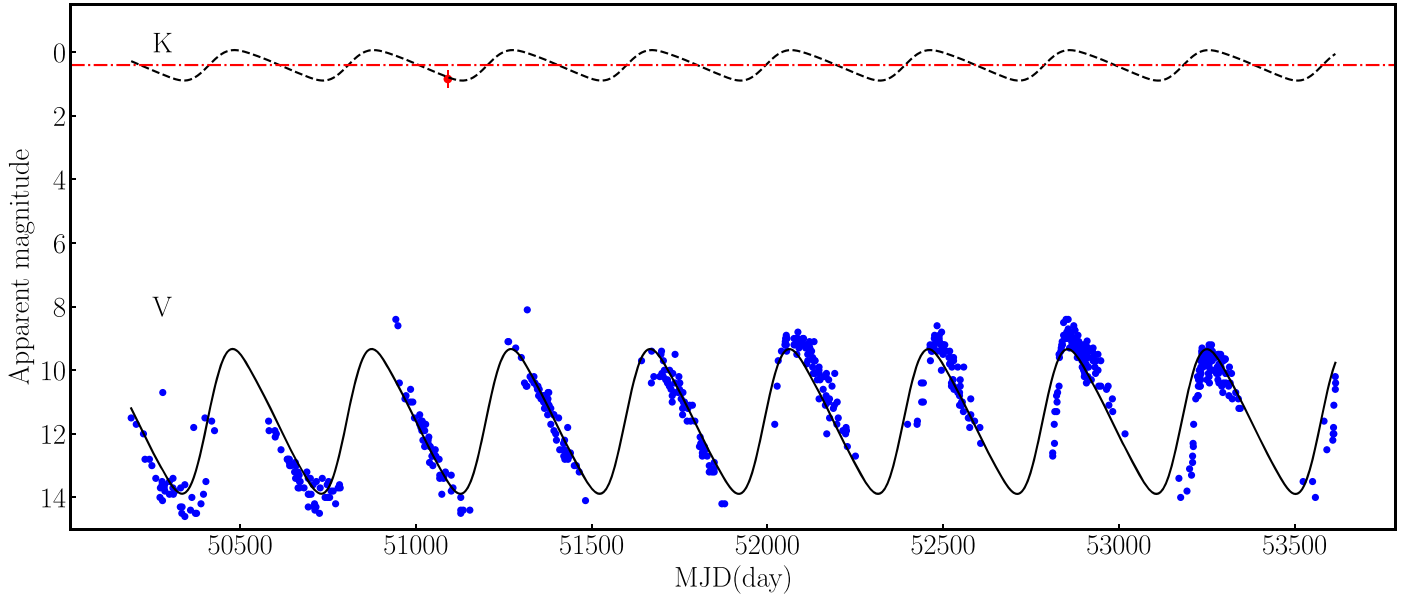
Figure 9. The light curve at optical *V* (*lower panel*) and a model near-infrared *K*-band (*upper panel*) for RR Aql (here only the data from 1996 to 2005 are presented for clarity). The single-epoch 2MASS datum is shown in red. The solid line shows the modeled optical light curve estimated by VStar. The dashed line shows the near-infrared light curve converted from the modeled optical light curve. The dashed–dotted line indicates the mean magnitude estimated by the lightcurve correction method for RR Aql.

with each other, with the VLBI value being more accurate. Compared with our Galactic PLR using VLBI parallaxes, the LMC zero-point derived by Yuan et al. (2017) differs by 0.13 mag. The PLR zero-point derived by Iwanek et al. (2021b) has a larger uncertainty and differs by 0.12 mag. All these zero-point differences are consistent within their joint uncertainties.

We derive "parallaxes" (from PLR-based distances) of 2.05 ± 0.31 mas and 2.45 ± 0.41 mas for RR Aql, using the LMC *K*-band PLRs of Yuan et al. (2017) and Iwanek et al. (2021b), respectively. While the latter PLR-based parallax is close to our VLBI parallax of 2.44 ± 0.07 mas; both are consistent within their uncertainties.

The scatter of PLR post-fit residuals listed in Table 7 for Galactic Miras is larger than for the LMC or M 33. Two likely reasons include (1) the Miras in other galaxies are at nearly the same distance, which removes distance uncertainty as a source of scatter, and (2) more than half of the Galactic Miras listed in Table 6 have only a single epoch of 2MASS magnitudes and these were measured with saturated detectors. The 2MASS apparent magnitude for these Miras at near-infrared *K*-band are brighter than 4th mag, which is the saturation limit for the 51 ms exposures, leading to larger magnitude uncertainty. Fluxes for these Miras were estimated by template fitting to the unsaturated scattered light in the wings of the saturated star

9

Table 6
Miras with Both VLBI and Gaia Parallaxes

Star	Π_{VLBI} (mas)	Π_{Gaia} (mas)	$\Pi_{VLBI}-\Pi_{Gaia}$ (mas)	Period (day)	m_K^{2MASS} (mag)	$m_K^{Kagoshima}$ (mag)	m_K^{mean} (mag)	$\sigma_{M_K}^{\Pi}$ (mag)	M_K^{VLBI} (mag)	M_K^{Gaia} (mag)	Maser	Array	References
(1)	(2)	(3)	(4)	(5)	(6)	(7)	(8)	(9)	(10)	(11)	(12)	(13)	(14)
Y Lib	0.86 ± 0.05	0.83 ± 0.08	0.03 ± 0.10	277	3.08 ± 0.29	3.25 ± 0.16		0.13	−7.08 ± 0.20	−7.15 ± 0.27	H₂O	VERA	k
X Hya	2.07 ± 0.05	2.53 ± 0.11	−0.46 ± 0.12	300	1.13 ± 0.28		1.03 ± 0.28	0.05	−7.39 ± 0.28	−6.95 ± 0.30	H₂O	VERA	e
R UMa	1.97 ± 0.05	1.75 ± 0.09	0.22 ± 0.10	302	1.11 ± 0.20	1.19 ± 0.02		0.06	−7.34 ± 0.06	−7.60 ± 0.11	H₂O	VERA	g
FV Boo	0.97 ± 0.06	1.01 ± 0.09	−0.04 ± 0.11	313	3.84 ± 0.27	2.91 ± 0.09		0.13	−7.15 ± 0.16	−7.06 ± 0.21	H₂O	VERA	i
R Cnc	3.84 ± 0.29	3.94 ± 0.18	−0.10 ± 0.34	357	−0.71 ± 0.17		−0.78 ± 0.17	0.16	−7.86 ± 0.24	−7.80 ± 0.20	H₂O	VERA	e
S CrB	2.39 ± 0.17	2.60 ± 0.11	−0.21 ± 0.20	360	−0.17 ± 0.17		−0.11 ± 0.18	0.15	−8.22 ± 0.24	−8.04 ± 0.20	OH	VLBA	c
T Lep	3.06 ± 0.04	3.09 ± 0.10	−0.03 ± 0.11	368	−0.27 ± 0.35		−0.57 ± 0.38	0.03	−8.14 ± 0.38	−8.12 ± 0.39	H₂O	VERA	e
S Ser	1.25 ± 0.04	0.77 ± 0.13	0.48 ± 0.14	372	1.68 ± 0.18		1.35 ± 0.24	0.07	−8.17 ± 0.25	−9.22 ± 0.44	H₂O	VERA	e
R Peg	2.76 ± 0.28	2.63 ± 0.12	0.13 ± 0.30	378	0.38 ± 0.36		0.68 ± 0.39	0.22	−7.12 ± 0.45	−7.22 ± 0.40	H₂O	VERA	e
R Hya	7.93 ± 0.18	6.74 ± 0.46	1.19 ± 0.50	380	−2.66 ± 0.19		−2.44 ± 0.22	0.05	−7.94 ± 0.23	−8.30 ± 0.27	H₂O	VERA	e
R Aqr	4.59 ± 0.24	2.59 ± 0.33	2.00 ± 0.41	390	−1.60 ± 0.33		−1.85 ± 0.35	0.11	−8.54 ± 0.37	−9.78 ± 0.45	SiO	VERA	e
W Leo	1.03 ± 0.02	0.88 ± 0.11	0.15 ± 0.11	392	1.80 ± 0.23		1.47 ± 0.27	0.04	−8.47 ± 0.27	−8.81 ± 0.38	H₂O	VERA	e
RR Aql	2.45 ± 0.08	1.95 ± 0.11	0.50 ± 0.14	396	0.84 ± 0.26		0.40 ± 0.33	0.07	−7.65 ± 0.34	−8.15 ± 0.35	H₂O	VLBA	d
U Her	3.76 ± 0.27	2.36 ± 0.08	1.40 ± 0.28	406	−0.63 ± 0.16		−0.55 ± 0.17	0.16	−7.67 ± 0.23	−8.69 ± 0.18	OH	VLBA	c
SY Scl	0.75 ± 0.03	0.52 ± 0.12	0.23 ± 0.13	411	2.65 ± 0.24		2.90 ± 0.27	0.09	−7.72 ± 0.28	−8.50 ± 0.57	H₂O	VERA	e
R Cas	5.67 ± 1.95	5.74 ± 0.20	−0.07 ± 1.96	430	−1.40 ± 1.00		−1.90 ± 1.03	0.75	−8.13 ± 1.27	−8.10 ± 1.03	OH	VLBA	a
AP Lyn	2.00 ± 0.04	2.02 ± 0.12	−0.02 ± 0.13	433	0.98 ± 0.20	0.60 ± 0.01		0.04	−7.90 ± 0.05	−7.87 ± 0.13	H₂O	VERA	h
U Lyn	1.27 ± 0.06	1.01 ± 0.08	0.26 ± 0.10	434	1.53 ± 0.23	1.15 ± 0.09		0.10	−8.33 ± 0.14	−8.82 ± 0.20	H₂O	VERA	f
BX Cam	1.73 ± 0.03	1.76 ± 0.10	−0.03 ± 0.11	486	0.91 ± 0.19	1.21 ± 0.11		0.04	−7.60 ± 0.12	−7.55 ± 0.17	H₂O	VERA	h
V837 Her	1.09 ± 0.02	0.18 ± 0.10	0.91 ± 0.10	520	2.06 ± 0.27	1.68 ± 0.03		0.04	−8.13 ± 0.05	−12.08 ± 1.25	H₂O	VERA	h
UX Cyg	0.54 ± 0.06	0.70 ± 0.09	−0.16 ± 0.11	565	1.40 ± 0.19		1.79 ± 0.26	0.24	−9.55 ± 0.35	−8.98 ± 0.39	H₂O	VLBA	b
OZ Gem	0.81 ± 0.04	0.45 ± 0.33	0.35 ± 0.33	598	3.00 ± 0.35	2.65 ± 0.16		0.11	−7.81 ± 0.19	−9.05 ± 1.55	H₂O	VERA	j

Note. Column 1 lists the names of Miras, columns 2 and 3 list VLBI and Gaia parallaxes, respectively, and column 4 lists VLBI and Gaia parallax differences. Column 5 lists the periods of magnitude variation at optical wavelength from AAVSO, except for V837 Her and AP Lyn, for which periods are from Chibueze et al. (2020). Apparent magnitudes at infrared K-band are listed in column 6, 7, and 8: m_K^{2MASS} values are from the 2MASS point-source catalog (Skrutskie et al. 2006), $m_K^{Kagoshima}$ are from the time-monitored observations with the Kagoshima University 1 m telescope and m_K^{mean} are the mean apparent magnitudes estimated using the lightcurve correction method. Adopted to calculate the absolute magnitude M_K (listed in columns 10 and 11) is $m_K^{Kagoshima}$ if available, otherwise m_K^{mean}. The uncertainties of M_K owing to VLBI parallax uncertainties are listed in column 9. The maser species are listed in column 12. The last two columns list the VLBI array for parallax measurements and references, respectively. The Gaia parallaxes are from Gaia Collaboration et al. (2021). The VLBI parallaxes are from (a) Vlemmings et al. (2003), (b) Kurayama et al. (2005), (c) Vlemmings & van Langevelde (2007), (d) this paper, (e) VERA Collaboration et al. (2020), (f) Kamezaki et al. (2016b), (g) Nakagawa et al. (2016), (h) Chibueze et al. (2020), (i) Kamezaki et al. (2016a), (j) Urago et al. (2020), (k) Chibueze et al. (2019), and (l) Kamezaki et al. (2014).
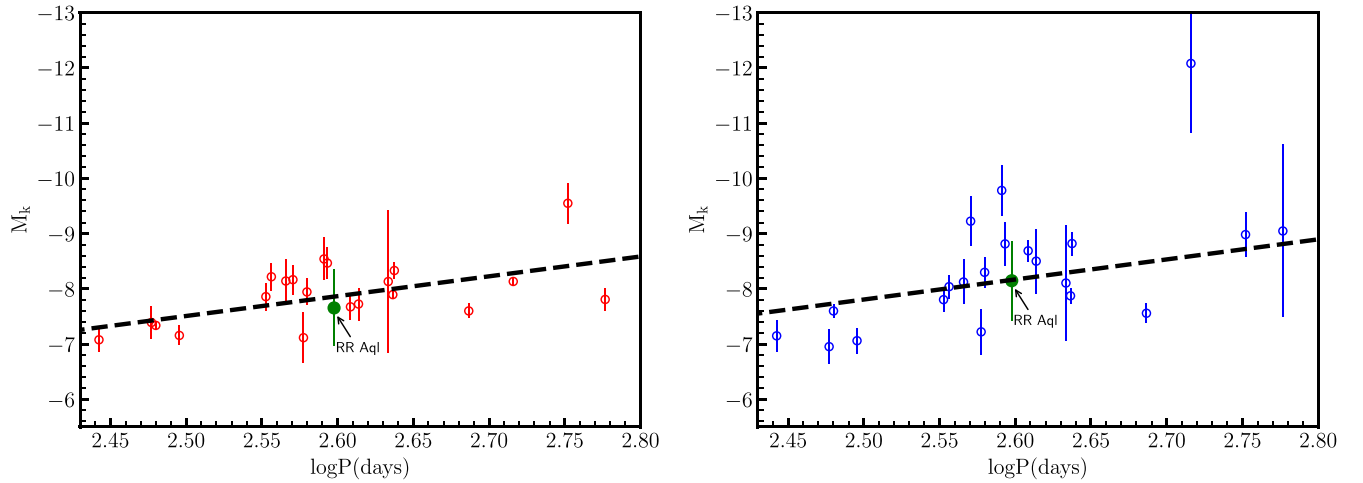
Figure 10. The PL(M_K) relation for Galactic Miras (dashed line) established in this paper using an "outlier tolerant" Bayesian MCMC approach, fitted to data from VLBI (*left panel*) and Gaia (*right panel*) parallaxes. The location of RR Aql on the PL diagram is given by a *filled circle* with its name.

Table 7
Coefficients of PLR of Miras at Near-infrared *K*-band in Different Galaxies

Galaxies	Slope (*a*)	Zero-point (*b*) (mag)	Scatter (mag)	*N*	References
(1)	(2)	(3)	(4)	(5)	(6)
LMC	−3.77 ± 0.07	−6.92 ± 0.04	0.12	158	Yuan et al. (2017)
M 33	[−3.77]	−6.97 ± 0.01	0.21	1169	Yuan et al. (2018)
LMC	−3.30 ± 0.46	−6.67 ± 0.06	0.27	29	Iwanek et al. (2021b)
Milky Way	−3.59 ± 0.29	−6.79 ± 0.15	0.45	22	This paper using VLBI parallaxes
Milky Way	−3.63 ± 0.30	−7.08 ± 0.29	0.94	22	This paper using Gaia parallaxes

Note. PLRs are defined as $M = a(\log P(\text{days}) - 2.30) + b$ for Miras at near-infrared *K*-band, matching those of Yuan et al. (2017, 2018) and Iwanek et al. (2021b). Columns 2 and 3 give the PLR slopes and zero-points. The Milky Way fits used a strong prior of −3.60 ± 0.30 for the slope and a very weak prior of −6.90 ± 1.00 mag for the zero-points. Columns 4 and 5 list the standard deviation of the post-fit residuals in magnitudes and the number of Miras fitted. The results for the LMC by Yuan et al. (2017) were based on Miras with periods <400 days, assuming distance modulus of 18.493 ± 0.048 mag (Pietrzyński et al. 2013); we have adjusted the zero-point and its uncertainty to an updated distance modulus of 18.477 ± 0.026 mag (Pietrzyński et al. 2019). The slope of the PLR for *M* 33 by Yuan et al. (2018) was fixed at −3.77 to match the LMC slope determined by Yuan et al. (2017). The PLR for the LMC by Iwanek et al. (2021b) assumed a distance modulus of 18.477 ± 0.026 mag (Pietrzyński et al. 2019); the zero-point uncertainty includes both the statistical and systematic errors.

image (Skrutskie et al. 2006). An examination of Table 6, suggests a typical uncertainty of the mean apparent 2MASS magnitudes is ≈0.3 mag. Removing a scatter of this magnitude from the total scatter of 0.45 mag for the VLBI-calibrated PLR, we find a residual scatter of 0.34 mag (i.e., $\sqrt{0.45^2 - 0.3^2}$). This residual scatter is currently unaccounted for, but could come from slightly underestimated parallax uncertainties and/or intrinsic brightness variations over different stellar cycles.

6. Conclusions

We have measured the trigonometric parallax and proper motion of the Mira variable RR Aql using VLBA observations of its water and SiO masers. Our parallax is 2.44 ± 0.07 mas, which differs significantly from the Gaia EDR3 parallax of 1.95 ± 0.11 mas. We fitted the positions of SiO masers to a circle and obtained the absolute position of the central star. Comparing the absolute positions of RR Aql from VLBA and Gaia, we find agreement within their joint uncertainties.

Using 22 Miras, including RR Aql, which have both VLBI and Gaia parallaxes, we have derived separately PLRs of Miras at near-infrared *K*-band. The post-fit residuals using VLBI parallaxes are about half as large as those using Gaia parallaxes, suggesting that VLBI parallaxes are more accurate than Gaia parallaxes for Miras. Thus, VLBI astrometry should be effective to validate future Gaia results for Miras.

Compared with the PLRs for Miras in other galaxies, the Galactic PLR based on the VLBI and Gaia parallaxes are statistically consistent with PLRs in the LMC and M 33 at near-infrared *K*-band. Since Miras vary by about 1 mag at infrared *K*-band, absolute magnitudes of Miras are uncertain by about ±0.4 mag when photometry from only a single epoch is used. This often dominates over parallax uncertainty when estimating absolute magnitudes. Thus, priority should be given to monitoring surveys of Miras at infrared *K*-band in order to obtain accurate measurements of mean m_K. Lacking multi-epoch magnitudes, combining optical light curves with infrared magnitudes can help to reduce the uncertainty due to the periodic variation.

In the era of space infrared telescopes, e.g., JWST, one could obtain extremely accurate apparent magnitudes for Miras. In addition, future astrometric results of Gaia, which could be validated by VLBI observations, are expected to greatly

increase the number of Miras with accurate parallaxes. More reliable Galactic PLRs of Miras will be available, leading to Miras being widely used as distance indicators.

ORCID iDs

Yan Sun https://orcid.org/0000-0002-8604-5394
Bo Zhang https://orcid.org/0000-0003-1353-9040
Mark J. Reid https://orcid.org/0000-0001-7223-754X

References

Benson, P. J., Little-Marenin, I. R., Woods, T. C., et al. 1990, ApJS, 74, 911
Chiavassa, A., Pasquato, E., Jorissen, A., et al. 2011, A&A, 528, A120
Chibueze, J. O., Omodaka, T., Urago, R., et al. 2019, PASJ, 71, 92
Chibueze, J. O., Urago, R., Omodaka, T., et al. 2020, PASJ, 72, 59
Deller, A. T., Tingay, S. J., Bailes, M., & West, C. 2007, PASP, 119, 318
Eyer, L., & Cuypers, J. 2000, in ASP Conf. Ser. 203, IAU Colloq. 176: The Impact of Large-Scale Surveys on Pulsating Star Research, ed. L. Szabados & D. Kurtz (San Francisco, CA: ASP), 71
Feast, M., & Whitelock, P. A. 2014, IAUS, 298, 40
Ferraz-Mello, S. 1981, AJ, 86, 619
Gaia Collaboration, Brown, A. G. A., Vallenari, A., et al. 2021, A&A, 649, A1
Glass, I. S., & Lloyd Evans, L. 1981, Natur, 291, 303
Huang, C. D., Riess, A. G., Hoffmann, S. L., et al. 2018, ApJ, 857, 67
Huang, C. D., Riess, A. G., Yuan, W., et al. 2020, ApJ, 889, 5
Iwanek, P., Soszyński, I., & Kozłowski, S. 2021a, ApJ, 919, 99
Iwanek, P., Kozłowski, S., Gromadzki, M., et al. 2021b, ApJS, 257, 23
Kamezaki, T., Kurayama, T., Nakagawa, A., et al. 2014, PASJ, 66, 107
Kamezaki, T., Nakagawa, A., Omodaka, T., et al. 2016a, PASJ, 68, 75
Kamezaki, T., Nakagawa, A., Omodaka, T., et al. 2016b, PASJ, 68, 71
Karovicova, I., Wittkowski, M., Boboltz, D. A., et al. 2011, A&A, 532, A134
Kemball, A. J., & Diamond, P. J. 1997, ApJL, 481, L111
Kurayama, T., Sasao, T., & Kobayashi, H. 2005, ApJL, 627, L49
Lacour, S., Thiébaut, E., Perrin, G., et al. 2009, ApJ, 707, 632
Lindegren, L. 2020, A&A, 637, C5
Lindegren, L., Klioner, S. A., Hernández, J., et al. 2021, A&A, 649, A2
Nakagawa, A. 2009, in AGB Stars and Related Phenomena, ed. A. G. B. Ueta, N. Matsunaga, & Y. Ita (Tokyo: National Astronomical Observatory of Japan), 58
Nakagawa, A., Kurayama, T., Matsui, M., et al. 2016, PASJ, 68, 78
Pietrzyński, G., Graczyk, D., Gieren, W., et al. 2013, Natur, 495, 76
Pietrzyński, G., Graczyk, D., Gallenne, A., et al. 2019, Natur, 567, 200
Reid, M. J., Braatz, J. A., Condon, J. J., et al. 2009, ApJ, 695, 287
Reid, M. J., & Honma, M. 2014, ARA&A, 52, 339
Reid, M. J., & Menten, K. 1991, in ASP Conf. Ser. 16, Atoms, Ions and Molecules: New Results in Spectral Line Astrophysics, ed. A. D. Haschick & P. T. P. Ho (San Francisco, CA: ASP), 375
Reid, M. J., & Menten, K. M. 1997, ApJ, 476, 327
Richards, A. M. S., Assaf, K, Bains, I., et al. 2010, in 10th European VLBI Network Symposium and EVN Users Meeting: VLBI and the New Generation of Radio Arrays (Trieste: PoS), 005
Sivia, D. S., & Skilling, J. 2006, Data Analysis-A Bayesian Tutorial (2nd edn; Oxford: Oxford Univ. Press)
Skrutskie, M. F., Cutri, R. M., Stiening, R., et al. 2006, AJ, 131, 1163
Urago, R., Yamaguchi, R., Omodaka, T., et al. 2020, PASJ, 72, 57
van Leeuwen, F. 2007, A&A, 474, 653
van Moorsel, G., Kemball, A., & Greisen, E. 1996, in ASP Conf. Ser. 101, Astronomical Data Analysis Software and Systems V, ed. G. H. Jacoby & J. Barnes (San Francisco, CA: ASP), 37
VERA Collaboration, Hirota, T., Nagayama, T., et al. 2020, PASJ, 72, 50
Vlemmings, W. H. T., & van Langevelde, H. J. 2007, A&A, 472, 547
Vlemmings, W. H. T., van Langevelde, H. J., Diamond, P. J., Habing, H. J., & Schilizzi, R. T. 2003, A&A, 407, 213
Whitelock, P. A., Feast, M. W., & van Leeuwen, F. 2008, MNRAS, 386, 313
Willson, L. A. 1981, in IAU Colloq. 59: Effects of Mass Loss on Stellar Evolution, ed. C. Chiosi & R. Stalio (Dordrecht: Reidel), 353
Wood, P. R. 2000, PASA, 17, 18
Xu, S., Zhang, B., Reid, M. J., Zheng, X., & Wang, G. 2019, ApJ, 875, 114
Yoon, D.-H., Cho, S.-H., Yun, Y., et al. 2018, NatCo, 9, 2534
Yuan, W., Macri, L. M., He, S., et al. 2017, AJ, 154, 149
Yuan, W., Macri, L. M., Javadi, A., Lin, Z., & Huang, J. Z. 2018, AJ, 156, 112